Journal of Geophysical Research: Solid Earth

RESEARCH ARTICLE
10.1029/2017JB015316

A Bayesian Method for Incorporating Self-Similarity Into Earthquake Slip Inversions

R. M. J. Amey[1], A. Hooper[1], and R. J. Walters[2]

[1]COMET, School of Earth and Environment, University of Leeds, Leeds, UK, [2]COMET, Department of Earth Sciences, Durham University, Durham, UK

Key Points:
- We present a method for incorporating fractal properties into earthquake slip inversions, using von Karman regularization
- Even when slip is not fractal, von Karman regularization retrieves the slip distribution at least as well as Laplacian regularization
- The von Karman solution for the 2014 M_w 6.0 Napa Valley earthquake gives tighter confidence bounds on slip than the Laplacian solution

Supporting Information:
- Supporting Information S1
- Table S1
- Table S2
- Table S3
- Movie S1

Correspondence to:
R. M. J. Amey,
eermja@leeds.ac.uk

Citation:
Amey, R. M. J., Hooper, A., & Walters, R. J. (2018). A Bayesian method for incorporating self-similarity into earthquake slip inversions. *Journal of Geophysical Research: Solid Earth, 123*, 6052–6071. https://doi.org/10.1029/2017JB015316

Received 4 DEC 2017
Accepted 5 JUN 2018
Accepted article online 25 JUN 2018
Published online 17 JUL 2018

Abstract Distributions of coseismic slip help illuminate many properties of earthquakes, including fault geometry, stress changes, frictional properties, and potential future hazard. Slip inversions take observations and calculate slip at depth, but there are a number of commonly adopted assumptions such as minimizing the second spatial derivative of slip (the Laplacian) that have little physical basis and potentially bias the result. In light of growing evidence that fault slip shows fractal properties, we suggest that this information should be incorporated into slip inversions as a form of regularization, instead of Laplacian smoothing. We have developed a Bayesian approach to efficiently solve for slip incorporating von Karman regularization. In synthetic tests, our approach retrieves fractal slip better than Laplacian regularization, as expected, but even performs comparably, or better, when the input slip is not fractal. We apply this to the 2014 M_w 6.0 Napa Valley earthquake on a two-segment fault using Interferometric Synthetic Aperture Radar (InSAR) and Global Positioning System (GPS) data. We find the von Karman and Laplacian inversions give similar slip magnitude but in different locations, and the von Karman solution has much tighter confidence bounds on slip than the Laplacian solution. Differences in earthquake slip due to the regularization technique could have important implications for the interpretation and modeling of stress changes on the causative and neighboring faults. We therefore recommend that choice of regularization method should be routinely made explicit and justified and that von Karman regularization is a better default than Laplacian.

1. Introduction

Determining the magnitude and distribution of slip along a fault plane is an essential component of earthquake investigations. Coseismic slip can help elucidate the geometry, strength, and frictional properties of active faults (Milliner et al., 2015; Perrin et al., 2016) and can be used to estimate where stress has been partially released and where it remains or has increased, which may indicate areas of the fault or neighboring faults that have been brought closer to or further from failure (Avouac et al., 2015; Lorito et al., 2011; Walters et al., 2009). The same inversion methods can also be used to monitor postseismic and interseismic slip (e.g., Floyd et al., 2016) and to help deduce the distribution and proportion of off-fault deformation, giving insight into the earthquake cycle (Lindsey & Fialko, 2016; Wang et al., 2015). Values of slip are also used extensively in palaeoseismic studies to estimate the magnitude of preinstrumental earthquakes (Campbell et al., 2015).

By combining satellite acquisitions before and after an earthquake, InSAR (Interferometric Synthetic Aperture Radar) provides spatially dense measurements of surface displacement, which along with Global Positioning System (GPS) measurements can be used to invert for the magnitude, location, and direction of earthquake slip along a fault plane. With the new European Space Agency satellites Sentinel-1A and Sentinel-1B providing unprecedented ground repeat times, the scientific community is now in a position to routinely investigate all large continental earthquakes using InSAR (Elliott et al., 2015), and inverting for slip is a crucial part of that procedure. However, in order for slip inversions to be useful we need to ensure that the inversion processes give results that adequately represent the true slip distribution.

Slip inversions are usually ill posed and unstable, meaning that the solution is nonunique and small amounts of data noise lead to slip oscillations in least squares solutions. Because of this inversions are usually regularized, with Laplacian smoothing being the most common approach (Funning et al., 2005; Harris & Segall, 1987; Wright, 2003). This regularization approach minimizes the second derivative of slip with the importance

of this constraint relative to minimizing data misfit controlled by a scalar smoothing factor. The choice of smoothing factor is often subjective and often not stated at all in the literature but can result in major differences between solutions derived from the same data. There is no specific justification for the use of Laplacian smoothing in slip inversions other than that a rough or oscillating slip distribution would produce unrealistically large stress drops. While Laplacian smoothing can prevent such large stress drops, this does not mean it is the best function to describe the nature of slip; it is just a mathematical constraint rather than being based on any observed fundamental feature of slip distributions.

Other regularization techniques promote sparse solutions (Evans & Meade, 2012) or impose little regularization (Jolivet et al., 2014; Minson et al., 2013), and these approaches, together with smoothness-promoting methods produce a huge range in solutions for the same earthquake. We argue that whichever regularization method is used, it should have a physical justification based on some observed behavior of earthquakes and faulting.

Many features of earthquakes and faults show self-similar (fractal) properties, meaning that a feature is similar at all scales or mathematically that a behavior can be described by a power law (Mandelbrot, 1983). Features that show this relationship include the Gutenberg-Richter frequency magnitude scale (Gutenberg & Richter, 1955; Kanamori & Anderson, 1975), the Omori aftershock frequency law (Omori, 1894), seismicity distribution across faults (Powers & Jordan, 2010), spatial structure of faults (Aviles et al., 1987; Okubo & Aki, 1987), spatial distribution of earthquake hypocenters (Robertson et al., 1995), fault gouge texture (Muto et al., 2015), fracture energy (Passelègue et al., 2016), and many others (see Ben-Zion (2008)).

Fault surfaces are naturally rough, and early work found this roughness is self-similar (Brown & Scholz, 1985; Poon et al., 1992; Power et al., 1988), meaning that the root-mean-square (RMS) height fluctuations are proportional to the profile length (Fang & Dunham, 2013). Recent higher-resolution studies of exhumed faults (Brodsky et al., 2011; Candela et al., 2012; Renard et al., 2006; Sagy et al., 2007) support these initial observations but find that roughness is self-affine rather than self-similar. Self-affine systems require different scaling in the x and z direction to maintain their similarity, where self-similar systems have the same scaling. In the context of fault roughness, a profile of fault topography is self-affine if it remains statistically invariant if the x (along-strike) and z (topography) coordinates are subject to the scaling transformation $\delta x \rightarrow \lambda \delta x$, $\delta z \rightarrow \lambda^H \delta z$, where H is the Hurst parameter (Candela et al., 2012). For a self-similar system, the scaling is instead λ in both directions i.e., H = 1. Different values of H are found along-strike and downdip directions, giving rise to different properties perpendicular and parallel to the slip vector.

Modeling of slip on a surface with fractal roughness predicts that both the distribution of stress drop and coseismic slip should also have a fractal distribution (Candela et al., 2011). Milliner et al. (2015, 2016) observed this in their field investigations of surface slip of the Landers earthquake rupture, where a power law describes the relationship between slip amplitude and wavelength. Models that produce power law frequency magnitude statistics of earthquake occurrence, in keeping with the Gutenberg-Richter law, also produce fractal slip distributions (Fisher et al., 1997).

Additionally, Mai and Beroza (2002) found that seismological slip solutions show fractal properties, a feature that was robust irrespective of the regularization imposed upon the inversions. They tested various autocorrelation functions to assess how the magnitude of slip varied as a function of distance and found that the von Karman autocorrelation function best describes slip distributions. This function has a similar power law relationship as a fractal distribution at high spatial frequencies, but the power decays more slowly for small wave numbers (large wavelength).

These studies imply that a better and more realistic alternative to regularization by Laplacian smoothing is regularization by constraining the slip distribution to be self-affine. By using a regularization technique that does not capture the fractal nature of slip we may be biasing slip solutions and therefore also any conclusions drawn from them. Fractal fault roughness is now incorporated into many numerical models of dynamic rupture (Bruhat et al., 2016; Fang & Dunham, 2013; Parsons & Minasian, 2015; Shi & Day, 2013) and ground-motion simulations (Mai et al., 2017), and in this paper we incorporate the von Karman autocorrelation function into a geodetic slip inversion as a prior assumption, using Bayesian methods.

The von Karman correlation was first introduced in fluid dynamics to describe turbulence (von Kármán, 1948). Unlike a fractal correlation that has only a single term to describe its power (the fractal dimension, D), the von Karman distribution also has correlation lengths, which define the cutoff lengths of fractal behavior

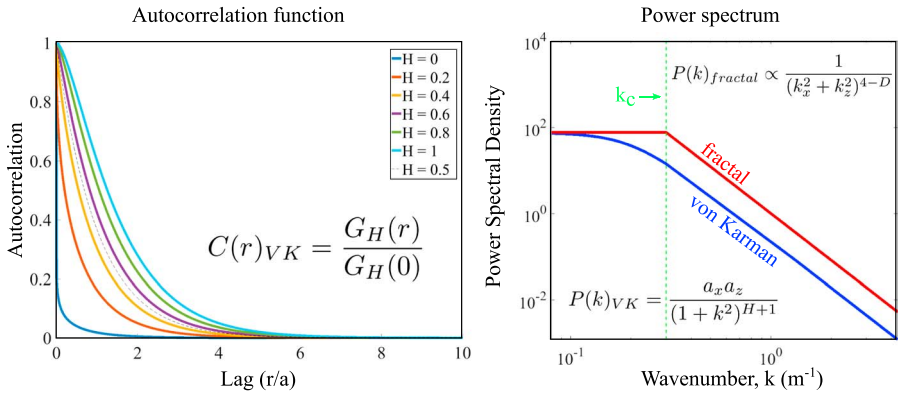

Figure 1. Left: the von Karman autocorrelation function, $C(r)$. The autocorrelation (similarity) between two functions decays with lag (scaled distance) between them. The exact shape of the drop-off is controlled by the Hurst parameter, H, where $H = 0.5$ is equivalent to an exponential decay function. Right: von Karman power spectrum, $P(k)$, using $a_x = 5$, $a_z = 15$, and $H = 0.8$ at $k_z = 0$. Also plotted at $k_z = 0$ is the fractal power spectrum, again using $H = 0.8$, giving a fractal dimension $D = E + 1 - H = 2.2$. For high wave numbers both are a straight line on the log-log graph, displaying characteristic self-similar properties. The fractal power spectrum decays beyond a corner wave number, $k_c = 0.3$, which is related to the characteristic source dimension (Mai & Beroza, 2002) whereas the von Karman shows a more gradual roll-off, the start of which is related to the correlation lengths, a_x and a_z. Here a_x and a_z were chosen to align the two functions at small wave numbers. Adapted from Mai and Beroza (2002).

(Dolan et al., 1998) and allow for different scalings downdip and along-strike, which is useful for capturing the nature of slip.

Here we use the von Karman distribution to describe the expected similarity of magnitude of slip between all patches of the fault. This correlation function, $C(r)$ is given by

$$C(r) = \frac{G_H(r/a)}{G_H(0)} \tag{1}$$

where $G_H(r/a) = (r/a)^H K_H(r/a)$, where K_H is a modified bessel function of the second kind, of order H; r is the distance between slip patches; a is the correlation length used to scale this distance; and H is the Hurst parameter (Mai & Beroza, 2002). The Hurst parameter describes the fractal properties of the correlation and controls the decay of this correlation (Figure 1). For self-affine profiles the Hurst parameter is linked to the fractal dimension, D, by D = (Euclidian dimension +1 − H) and is a measure of the long-term memory of a system.

In form, the von Karman correlation decays as a function of lag (scaled distance), and for $H = 0.5$ the von Karman function is identical to an exponential decay function. The von Karman correlation decays quicker for either decreased Hurst parameter or decreased correlation lengths. Thus, the correlation between the magnitude of slip on two patches decays as a function of the distance between them, and the nature of this decay is controlled by the Hurst parameter and correlation lengths.

The von Karman correlation can be added as a prior assumption into a slip inversion, so that a slip solution has a joint probability based upon how well a slip distribution fits the observed data and how well the slip distribution fits the von Karman autocorrelation function. The parameters describing the von Karman distribution (H and a) could themselves be solved for as hyperparameters, with their prior probability distributions determined by the seismic study meta-analysis from Mai and Beroza (2002). These parameters differ depending on fault type (normal, reverse, or strike slip) and also differ in the along-strike and downdip directions.

In this study we present a method to invert for slip incorporating von Karman regularization, using a Bayesian approach and implemented using a Markov chain Monte Carlo (MCMC) algorithm. A Bayesian approach allows us to fully explore the range of parameters that fit the data, incorporate constraints (e.g., on rake to avoid unphysical features such as back slip), and solve for a hyperparameter that represents the variance of the slip (discussed more in section 2.3). This means that instead of having to assume in advance the variance of slip we are able to search the range of slip magnitudes and rakes for a range of permitted variances. This flexible approach, while computationally expensive, allows us to be more objective and explore the full range of possible solutions in more detail.

We test this method on synthetic data and then apply it to the M_w 6.0 Napa Valley, California, 2014 earthquake. For comparison we also invert for slip with Laplacian smoothing implemented using the same Bayesian approach.

2. Method and Data

2.1. Bayesian Inversion

In Bayesian inversions each parameter to be solved for (e.g., slip and rake) is treated as a random variable with a prior probability density function (PDF) that is updated by the inversion process. The result is the full joint posterior PDF for every model parameter, giving an ensemble of all possible models that fit the data reasonably, as well as providing a good understanding of the uncertainties on parameters and the covariance between them. This approach also allows us to solve for hyperparameters within the inversion.

Following Fukuda and Johnson (2008) and Hooper et al.'s (2013) incorporation of Laplacian smoothing into slip inversions using a nonlinear Bayesian approach, here we present our method for incorporating a von Karman prior assumption, after Hooper (2012).

The posterior probability is built from the prior and likelihood function using Bayes' theorem. The prior probability describes how well the model parameters fit a prior assumption. The likelihood function describes how well the forward model calculated using these model parameters fits the observed data.

Bayes' theorem states

$$p(\mathbf{m}|\mathbf{d}) = \frac{p(\mathbf{d}|\mathbf{m})p(\mathbf{m})}{\int_{-\infty}^{\infty} p(\mathbf{d}|\mathbf{m})p(\mathbf{m})d\mathbf{m}} \tag{2}$$

Meaning that the posterior probability, $p(\mathbf{m}|\mathbf{d})$, of a model, $\mathbf{m}$, given a set of data, $\mathbf{d}$, is the product of the prior probability of the model, $p(\mathbf{m})$, and the fit to data, $p(\mathbf{d}|\mathbf{m})$, where the denominator is a normalizing constant.

We use an MCMC method incorporating the Metropolis-Hastings algorithm to generate samples of the prior probability density and also to sample the parameter space and thus approximate the posterior PDF. The algorithm samples parameter space in such a way that more models are drawn in areas of high probability. We adapt the approach of Fukuda and Johnson (2008) to include multiple Metropolis steps and sensitivity tests.

An MCMC chain is a memoryless system in which parameter space is sampled using random walks, with each random step depending only upon the previous step (in contrast to methods such as the neighborhood algorithm; Sambridge, 1999). The MCMC chain samples parameter space to provide an estimation of the posterior PDF (Tarantola, 2005, Chapter 2, Page 50).

2.2. Our MCMC Approach

In an MCMC chain each parameter is perturbed at the start of each iteration, meaning a random number is added to each model parameter giving a new "trial" value. The new trial is drawn from the prior distribution, then the likelihood is calculated. The trial is then accepted or rejected using the "Metropolis rule." This acceptance rule states that if the trial likelihood is greater than that of the current model it is accepted. If the trial likelihood is lower, then the probability of acceptance is calculated: the ratio of the two likelihoods. This ratio is compared to a randomly drawn number between 0 and 1. If the probability of acceptance is greater than this random number, the trial is accepted. Otherwise, it is rejected. This means that sometimes trials that have lower likelihood are accepted, which allows the chain to not get stuck in local minima. If a trial is accepted it is saved; the next random step is taken from those model parameters.

At the end of the inversion the first B iterations that constitute the "burn-in" are removed. These are the early steps that do not properly sample the posterior as they may be influenced by starting state (Fukuda & Johnson, 2008). The rest of the saved trials represent the posterior, giving the full range of models that adequately fit the data and prior assumptions. This posterior can be represented by some statistical representation of the distribution, which is discussed further in section 4.3.

Here we implement the MCMC chain in two separate steps for efficiency, as described by Tarantola, (2005, Chapter 2, Page 52). The first step generates samples of the prior probability density: a von Karman trial. We draw random slip trials for each patch from their prior distribution (section 2.4) and use the Metropolis-Hastings algorithm to accept/reject these trials based on their von Karman probability. The slip trials are generated by adding a random number from a boxcar distribution between $\pm$ each

parameters' "step size." The second step is to sample the posterior probability distribution, which is achieved by comparing the likelihoods of the current trial to the previous trial (Tarantola, 2005, Chapter 2, Page 52). This implementation reduces the number of times the particularly computationally expensive likelihood calculation is made, since it avoids making the calculation for most models that already have a low posterior probability due to their slip distribution having very low von Karman probability. Also for efficiency we periodically perform a sensitivity test to adapt the step sizes being taken, which is discussed in detail in section 2.6. In section 2.4 we describe how we sample the prior and in section 2.5 we describe how we sample the posterior, using the likelihood; these two steps together comprise one iteration of our algorithm.

2.3. Model Parameterization

We divide the fault into M slip patches and solve for magnitude of slip and rake (the direction of slip) separately for each patch, as well as a hyperparameter α^2 for each separate fault. The physical meaning of the hyperparameter α^2 is the variance of the slip. The correlation matrix calculated using equation (1) defines the desired von Karman correlation between slipping patches and the hyperparameter α^2 acts on this to dictate the magnitude of the slip, in effect converting correlation to variance-covariance. It is necessary to solve for α^2 in order to explore the full plethora of slip and rake solutions that fit a range of permitted variances. If a model contains multiple faults that are assumed to be uncorrelated in terms of their slip, then we would calculate separate von Karman prior probabilities for each fault and consequently we assign one α^2 parameter per fault. Slip and α^2 are the only parameters used in the von Karman prior probability calculation.

2.4. First MCMC Step—Sampling the Prior

The prior probability describes how well a slip distribution fits the prior assumptions. Here the prior is the product of prior distributions of slip magnitude and rake for individual patches, α^2 for each separate fault, the von Karman probability of slip and a moment regularization (if this option is used).

2.4.1. Model Parameter Priors

We solve for slip magnitude and rake using boxcar priors, and we solve for α^2 using a logarithmic prior. This means that for slip and rake the new trials are generated with uniform probability between a given range, that is, slip is given uniform probability between 0 and x meters, and the probability is 0 outside of this range. For α^2 we implement a logarithmic prior. This means that we solve for a model parameter, q, and then calculate α^2 by $\alpha^2 = 10^q$, thus transforming a uniform prior for q into a logarithmic prior for α^2.

2.4.2. Von Karman Prior

Once each model parameter has been drawn from its prior, we apply the von Karman prior using the Metropolis-Hastings algorithm, since it is difficult to directly generate von Karman distributions directly with a random walk.

The von Karman autocorrelation is given by:

$$p(\mathbf{s}) = (2\pi\alpha^2)^{-M/2}|\mathbf{\Sigma_s}|^{-1/2}e^{\frac{-1}{2\alpha^2}\mathbf{s}^T\mathbf{\Sigma_s}^{-1}\mathbf{s}} \tag{3}$$

where

$p(\mathbf{s})$ = probability of this slip distribution
α^2 = a hyperparameter controlling the slip variance
M = number of slip patches in a fault strand
$|\mathbf{\Sigma_s}|$ = the determinant of the slip patch autocorrelation matrix
$\mathbf{s}$ = vector of slip magnitudes

We calculate the probability for each separate fault using a corresponding α^2 term for that strand. The product of the prior probabilities for all the faults gives the the joint probability of the overall distribution of slip conforming to the von Karman correlation function.

The autocorrelation, $\mathbf{\Sigma_s}$, is calculated for a particular fault strand from the von Karman correlation function given in equation (1). In MATLAB, $G_H(0)$ gives an infinite value, so we investigated the $\lim_{r\to 0}$ of $G_H(r) = (r)^H K_H(r)$. We found any values smaller than $r = 10^{-4}$ changed the value of $G_H(r)$ significantly less than 1% so we therefore used a value of $r = 10^{-10}$ to approximate $r = 0$.

We calculate the scaled distance, r/a, by calculating the along-strike and downdip separation distance between each fault patch, then dividing this by the along-strike, a_{as}, or downdip, a_{dd}, correlation value, respectively. We then used these scaled along-strike and downdip separation distances to calculate the scaled

separation distance between each patch. We used the correlation values from Mai and Beroza (2002) for strike-slip faults:

$$a_{as} = 1860 + 0.34 \times (\text{fault length; meters}) \tag{4}$$

$$a_{dd} = -390 + 0.44 \times (\text{fault width; meters}) \tag{5}$$

We also used Hurst parameter values, H, from Mai and Beroza (2002) for along-strike, $H_{as} = 0.71$, and downdip, $H_{dd} = 0.77$ and scaled them appropriately for angles between purely along-strike and downdip. These correlation lengths and Hurst parameters could be solved for as hyperparameters as part of the inversion in future studies.

2.4.3. Moment Regularization Prior

Geodetic slip inversions have poor depth resolution since all the data are acquired at the surface. Consequently deep slip makes very little difference to the likelihood; it is almost in the null space. To attempt to limit the amount of slip being put in the null space we optionally include moment regularization in the inversion such that slip trials with a moment very different to that of the seismological moment are more likely to be rejected. We use a Gaussian prior for moment: it is calculated with the standard equation for calculating the probability from a Gaussian distribution given a mean (moment from the U.S. Geological Survey [USGS] page) and standard deviation (standard deviation of the different moment calculations on the USGS page). The prior probability is then the von Karman prior multiplied by the moment regularization prior.

However, we prefer to avoid this regularization where possible, since many geodetic measurements also include surface displacements from postseismic slip or aftershocks, and there are often systematic differences between geodetically and seismologically derived seismic moments (Weston et al., 2011). It is not clear whether this is predominantly due to real differences from aseismic slip, errors in the seismic estimate or errors in the geodetic estimate, or some combination of these. In this study moment regularization is not applied unless specifically mentioned.

2.4.4. Prior Acceptance Rule

We use the Metropolis rule to decide if a temporary trial is accepted, as discussed in section 2.2. If it is accepted then it is a representative draw from the von Karman distribution and the other prior distributions; therefore, we move onto the second step.

2.5. Second MCMC Step—Sampling the Posterior

Once we have drawn a sample from the prior using the first MCMC step, we sample the posterior by calculating the likelihood.

A forward model of surface displacements is calculated from the trial model parameters, using the formulation for rectangular dislocations in an elastic half space (Okada, 1985). This is calculated by multiplying the current slip model, $\mathbf{s}$, by a kernel $\mathbf{G}$, which gives predicted surface displacements, $\hat{\mathbf{d}}$, at each of the locations of our InSAR and GPS data for unit slip on each fault patch and the appropriate rake:

$$\hat{\mathbf{d}} = \mathbf{Gs} \tag{6}$$

Because we solve for slip magnitude and rake, the kernel $\mathbf{G}$ needs to be updated for the current rake value during each iteration. For a linear case in which fault geometry is held fixed (i.e., not changing dip), $\mathbf{G}$ matrices for purely left-lateral strike slip, $\mathbf{G}_{ss}$, and purely thrust dip slip, $\mathbf{G}_{ds}$, movement can be calculated before commencing the inversion. Then the $\mathbf{G}$ matrix for the current iteration is calculated using the current values of rake by:

$$\mathbf{G} = \mathbf{G_{ss}} \times \cos(\text{rake}) + \mathbf{G_{ds}} \times \sin(\text{rake}) \tag{7}$$

where cos(rake) and sin(rake) are diagonal matrices.

The likelihood is calculated using the weighted misfit of a forward model to the observed data. The misfit is weighted by the inverse of the variance-covariance matrix, $\mathbf{\Sigma_d}$, which represents data uncertainty. The likelihood is given by:

$$p(\mathbf{d}|\mathbf{m}) = (2\pi)^{-N/2}|\mathbf{\Sigma}_{\boldsymbol{d}}|^{-1/2} e^{\frac{-1}{2}(\mathbf{d}-\mathbf{Gs})^T \mathbf{\Sigma}_{\boldsymbol{d}}{}^{-1}(\mathbf{d}-\mathbf{Gs})} \tag{8}$$

where

$p(\mathbf{d}|\mathbf{m})$= the probability of the observation, given the slip and rake distribution
N = total number of data points
$\mathbf{\Sigma_d}$ = variance-covariance of the data
$\mathbf{d}$ = data (e.g., InSAR, GPS,
$\mathbf{s}$ = magnitude of slip
$\mathbf{G}$ = kernel, calculated for the appropriate rake and dip values

We then once again use the Metropolis rule on the ratio of the trial likelihood to current model likelihood. If the trial passes this test, then it is saved as the current model and future trials will be drawn as a step from this trial, until another more likely trial is drawn. If the trial is rejected, the previous model is saved and next trial is initiated from this trial.

The inversion results in a joint probability from which we can calculate a histogram of the posterior for each model parameter. We can also calculate the 2-D PDFs that show the joint PDF of each pair of parameters.

2.6. Efficiency

Bayesian inversions are computationally expensive, and so methods are employed to improve the efficiency of the parameter search, such as the use of multiple MCMC chains, for example Minson et al. (2013). Here we improve efficiency by using two steps within one MCMC chain as discussed in section 2.2 and by modifying the step size for each parameter within the MCMC chain, in a manner similar to that used by Hooper et al. (2013) and also Minson et al. (2013) between chains.

We modify the step size for each parameter to achieve an optimal acceptance rate of 0.234 (Roberts et al., 1997). Acceptance rates that are higher or lower than this give an inefficient search of parameter space. For the sensitivity tests we use a "rejection" to mean either a rejection at the prior or likelihood stage.

In order to ensure we achieve this ideal rejection ratio while properly exploring parameter space, we perform sensitivity tests at regular intervals throughout the inversion, with the first sensitivity test, $j = 1$, starting at $i = 100$ where i is the iteration, then at $i = 500$ and every 1,000 iterations up until 10,000 and then every 10,000 iterations for higher values of i. We use a "probability target" parameter to adjust the step sizes, so that perturbation of each model parameter results in the same amount of change to the posterior probability. This probability target is the expected ratio of the posterior probability after perturbing a single model parameter, to the current posterior probability. Changing step sizes to match this probability target ensures no parameter is having too great or too little an effect on the posterior probability. Adapting the probability target with the rejection rate forces step sizes to increase or decrease to optimize efficiency. At the start of a sensitivity test we first adjust the probability target at the current sensitivity test, j, using the probability target from the previous sensitivity test, $j-1$, by

$$\text{Ptarget}_j = \text{Ptarget}_{j-1} \times \frac{r_{\text{ideal}}}{r_j} \tag{9}$$

This means if too many trials are being rejected (i.e., the rejection ratio since last sensitivity test, r_j, is larger than the ideal rejection ratio, r_{ideal}) then the previous probability target, Ptarget_{j-1}, will be decreased. We then adjust step sizes of each model parameter using this new probability target. This is done during a sensitivity test by calculating the posterior probability, perturbing each parameter by half a step size in turn and recalculating the posterior probability. The ratio of posterior-before-perturbation to posterior-after-perturbation is calculated and subtracted from the probability target to give the difference, D. If the perturbation is such that model parameter's contribution to the posterior probability is more than the probability target ($D < 0$) then the step size is having too large an effect, which means the step size must be decreased. We decrease or increase step sizes using the empirical formula:

$$\text{step size}_j = \text{step size}_{j-1} \times e^{\frac{D}{\text{Ptarget}_j \times C_1}} \qquad \text{for } D > 0 \text{ (step sizes too small)} \tag{10}$$

$$\text{step size}_j = \text{step size}_{j-1} \times e^{\frac{D}{(1-\text{Ptarget}_j) \times C_2}} \qquad \text{for } D < 0 \text{ (step sizes too big)} \tag{11}$$

where the constants, $C1$ and $C2$, are arbitrarily chosen to control how quickly step sizes increase or decrease in size; increasing C_1 decreases the amount by which step size increases; increasing C_2 increases the amount by which a step size decreases. These values were chosen after experimentation as they resulted in gradual

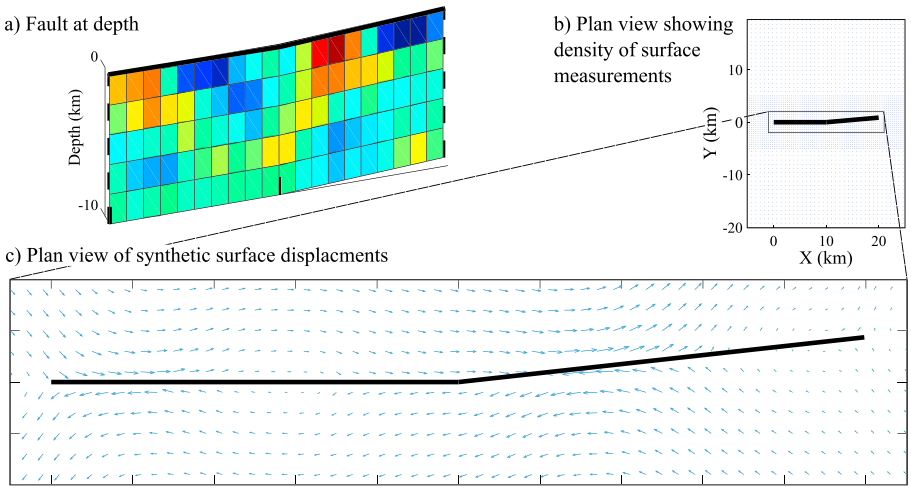

Figure 2. Set up of synthetic tests. (a) Fault plane, with two joining strands, with example slip distribution indicated by color. Thick black line shows top of fault, at the surface. (b) Plan view of location of surface displacements caused by this right-lateral fault, indicated by a black line. (c) Zoomed in on box shown in b, showing the surface displacements around the fault.

changes in rejection rates in synthetic tests. Different values may work better in different situations, depending on the number of model parameters. For a von Karman regularized inversion we use $C_1 = 16$ and $C_2 = 2$, although we find higher values of C_1 work better for Laplacian and moment regularized inversions. If we are re-running an inversion we optionally use the idealized step sizes from a previous run. A simple test demonstrates that an inversion scheme with changing step sizes correctly samples the posterior (supporting information Figure S1); a mathematical proof of this is beyond the scope of the current paper but would be a valuable avenue of future work.

3. Synthetic Tests

3.1. Synthetic Test Set Up

We first tested our slip inversion code on three synthetic cases. Each consists of a strike-slip fault modeled as two connected strands, and the simulated surface displacements are created using our forward model described by equation (6), shown in Figure 2. The three synthetic slip distributions created are

1. Uniform, pure strike-slip motion that ruptures the surface down to ~6 km depth.
2. Laplacian smoothed slip.
3. Slip displaying von Karman autocorrelation.

The Laplacian smoothed slip is created using a matrix of discretized Laplacians appropriate for this fault geometry, the inverse of which is multiplied by normally distributed random numbers.

The von Karman consistent synthetic test is created by transforming a random slip distribution into a correlated distribution using the appropriate correlation matrix (e.g., Lohman & Simons, 2005), for a fault of given dimensions.

To investigate the differences caused by regularization alone we conducted the synthetic tests on noise-free synthetic data. We used a high density of 3-D surface displacements, spaced every 400 m within 5 km of the fault and every 2 km up to a distance of 20 km from the center of the fault.

We then inverted for slip for these three separate synthetic tests using three modes of the Bayesian inversion: with no regularization, Laplacian regularization, and von Karman regularization.

Each was performed with the correct fault geometry, with a prior rake within $\pm 30^\circ$ of the true value, adding no further regularization than that specified above. For Laplacian regularization we solved for the hyperparameter that controls the strength of the smoothing within the inversion.

3.2. Synthetic Test Results

The results are shown in Figures 3 and 4, supporting information Figures S2 and S3, and the fit to the data for each model shown in supporting information Figures S4–S12.

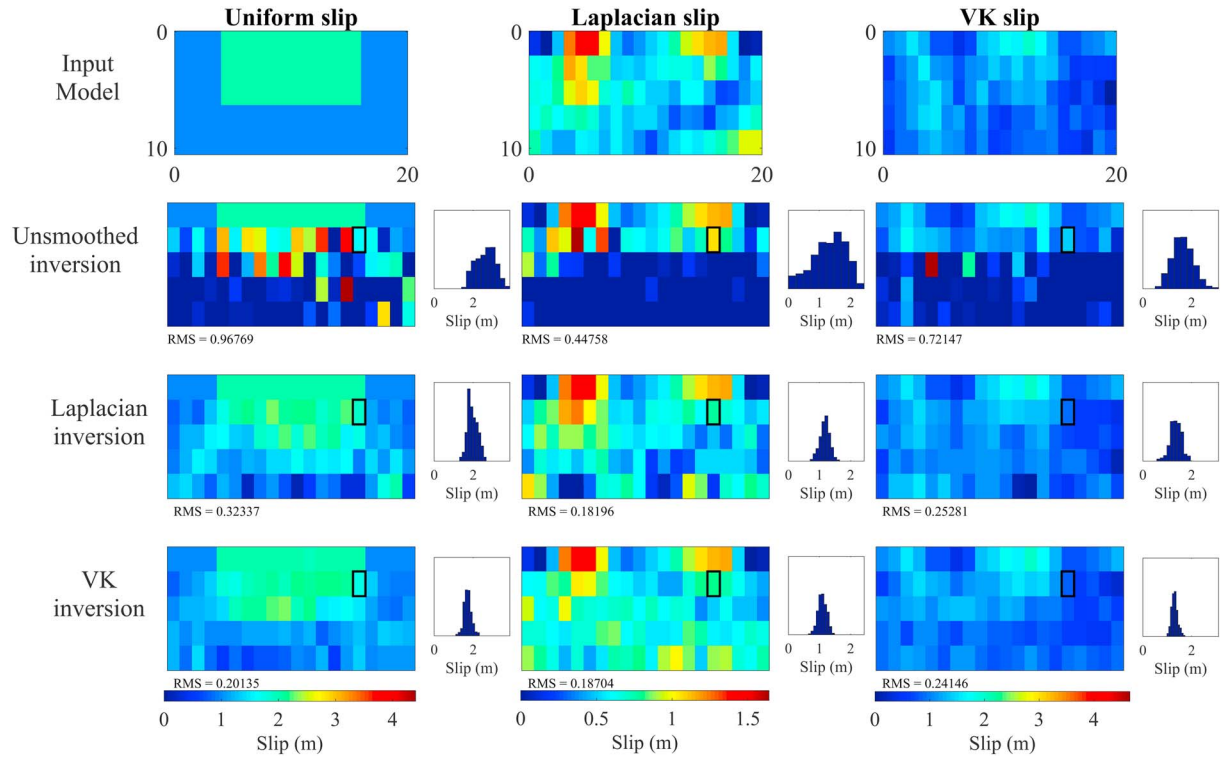

Figure 3. Results of slip inversions for synthetic tests, each with the fault planes shown as a flat surface and color indicating magnitude of slip. Top row shows input slip distribution, which is then solved using a Bayesian inversion with no smoothing (row 2), with Laplacian smoothing (row 3), and von Karman smoothing (row 4). All distributions displayed give the mode result for each patch and are displayed with the same color scale as the corresponding model. Note that the color bar for column 3 (von Karman [VK] slip) is saturated for one value in the unsmoothed solution. The root-mean-square is the sum of the square of the misfit between the true slip (input model) and the mode of each patch, not data misfit. Also shown is the PDF for patch 77, indicated by a box, showing how smoothed solutions give a much tighter constraint than unsmoothed versions.

It is not simple to display the results from a Bayesian inversion since the inversion produces a multidimensional joint PDF for all model parameters. All saved models formulate the solution, which would best be displayed as a video. However, to present the results in a 2-D image, in Figure 3 we have plotted the "mode" solution for each slip patch. This slip distribution itself has not been drawn as a trial in the Bayesian inversion but gives an indication of where slip is likely to have occurred from all the saved trials. We calculate the joint slip mode and rake mode for each patch by finding the value of the peak of the highest bar in the 2-D histogram of slip against rake.

All solutions fit the data very well; however, low data residuals do not ensure a correct source model, as the Earthquake-Source Inversion Validation project has previously shown (Mai et al., 2016). The smoothed solutions give a less oscillatory result than the unsmoothed solutions and also the unsmoothed solutions add additional high slip at depth; no moment regularization was applied to any of the synthetic test inversions.

These tests show that a von Karman correlation constraint retrieves a von Karman slip distribution better than a Laplacian or no constraint, as might be expected. However, von Karman also adequately resolves a slip solution that is not von Karman. The von Karman regularization outperforms both Laplacian regularized and unsmoothed inversions for uniform slip, as is shown by the lower RMS (text under each solution in Figure 3). For the Laplacian slip input model and von Karman slip input model the RMS for von Karman regularization and Laplacian smoothing is similar enough to suggest they have the same resolving power for these slip distributions ($RMS_{\text{Laplacian}} = 0.182$ and $RMS_{\text{vonKarman}} = 0.187$ for Laplacian slip, and $RMS_{\text{Laplacian}} = 0.252$ and $RMS_{\text{vonKarman}} = 0.241$ for von Karman slip.

Further comparisons using the method outlined by Zhang, Mai, et al. (2015) confirm this, shown in supporting information Figure S13. We find that the von Karman solution outperforms Laplacian and unsmoothed solutions in matching the magnitude of slip and correlation of slip for all three input slip distributions, though for Laplacian input slip, the von Karman is only marginally better than the Laplacian.

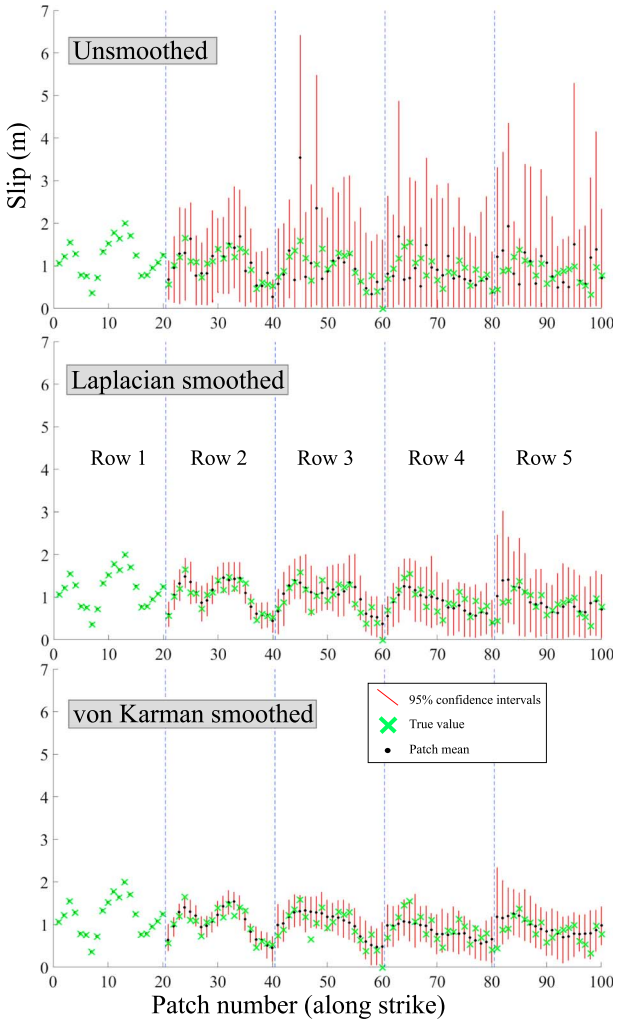

Figure 4. 95% confidence intervals (red line) for each slip patch, patch mean (black circle), and the true value for that slip patch (green cross) for von Karman slip solved for with no smoothing (top), Laplacian smoothing (middle), and von Karman smoothing (bottom). For von Karman regularization 94% of patches had the true value of slip within the 95% confidence intervals, compared to 99% for Laplacian smoothing. Note that Row 1 (the surface) has significantly smaller confidence intervals due to better resolving power nearer to the data, which means the patch mean and true slip are plotting in very similar locations, and confidence intervals are too small to see.

The histograms in Figure 3 show the posterior PDF for a single slip patch, indicated by the black box, for each of the different inversion methods. An unsmoothed inversion has a very high standard deviation in the histogram, showing that the slip is poorly constrained. In comparison, the smoothed solutions have much lower standard deviations, meaning they have a much tighter constraint. This is apparent in Figure 4 for von Karman slip and supporting information Figures S2 and S3 for surface slip and Laplacian slip, which show that the smoothed inversions yield much tighter confidence intervals than for the unsmoothed inversion. For von Karman slip the true value of slip lies within the 95% confidence intervals for 94 out of 100 patches using von Karman regularization and 99 out of 100 patches for Laplacian regularization.

3.3. InSAR/GPS Synthetic Test

We explored the effects that data type (InSAR and/or GPS) may have on the ability for a regularization style to resolve an input slip distribution. InSAR has the benefit of high spatial resolution, but the displacement field is only measured in one dimension (satellite line of sight). In contrast GPS provides 3-D measurements of displacement but at a spatially sparser set of discrete locations.

We created a synthetic test with noise-free InSAR data spaced every 400 m within 5 km of the fault, and every 2 km up to a distance of 20 km away from the fault, with the same line of sight vector as for the Sentinel-1 interferograms in the Napa earthquake. To simulate loss of coherence we randomly remove 800 data points, which also serves to reduce the time to calculate the likelihood. We randomly scattered thirty noise-free 3-D GPS measurements around the fault.

We simulated von Karman slip on a strike-slip fault consisting of two connected segments and solved for this with von Karman regularization and Laplacian smoothing.

We find that the von Karman regularization consistently matches the magnitude of input slip and spatial distribution of input slip better than Laplacian, regardless of data type used in the inversion (supporting information Figures S14 and S15).

3.4. Synthetic Test Summary

These tests demonstrate that our method is working as expected and that inversions incorporating von Karman regularization can successfully recover the distribution of slip from geodetic data.

Our new method of regularization not only outperforms Laplacian smoothing when the slip has a fractal distribution but also does better for uniform slip and performs comparably when slip is smooth. This suggests that incorporating von Karman regularization into slip inversions is likely to produce solutions that are at least as accurate than those generated by inversions incorporating Laplacian smoothing, and if the true slip conforms to the von Karman correlation function, our method is significantly more accurate. Therefore, it is a better default regularization approach to use than Laplacian.

4. M_w 6.0 Napa Valley Earthquake, 2014

We applied our method to the M_w 6.0 Napa Valley, California, earthquake of 24 August 2014. This was the first earthquake imaged by Sentinel-1A, with the preearthquake image acquired on the first day that the satellite reached its operational orbit. The earthquake occurred on the West Napa Fault (Hudnut et al., 2014), which is part of the San Andreas fault system; the broad region of faults that accommodates right-lateral movement between the Pacific and North American plates (Figure 5).

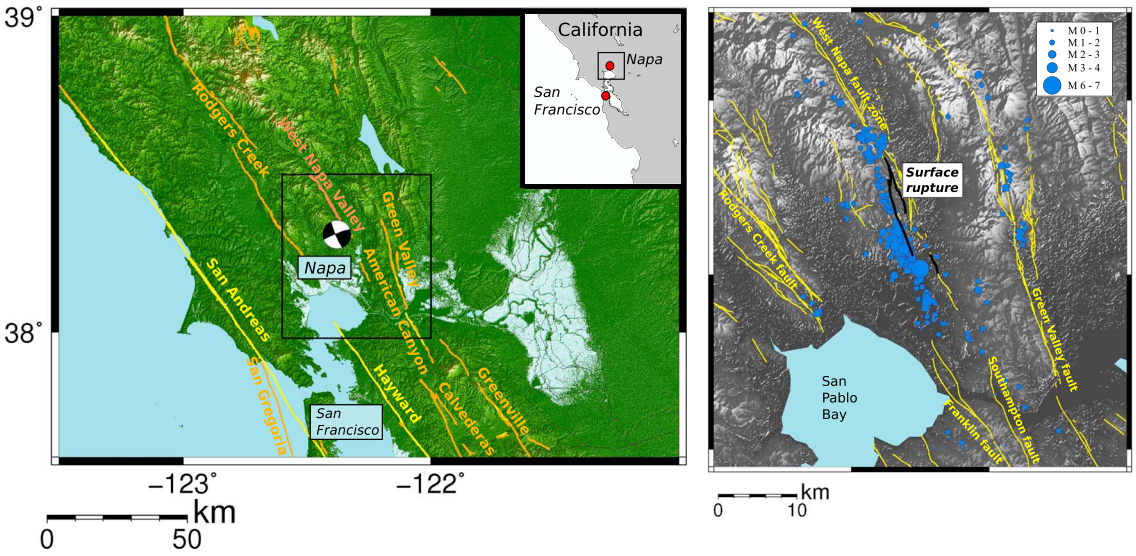

Figure 5. Regional setting of the Napa Valley earthquake. Left: Focal mechanism was almost entirely strike slip with a strike of 345°. Historical (yellow), Holocene (orange), and selected Quaternary (coral) faults (USGS, 2006). Right: surface rupture of Napa earthquake from (Hudnut et al., 2014) and aftershocks from August to February shown in blue, with size indicating magnitude. Yellow shows faults of all ages (USGS, 2006).

4.1. InSAR and GPS Data

The details of the acquisition and processing of the InSAR and GPS data are given in Floyd et al. (2016). The earthquake happened on 24 August 2014, and the second Sentinel-1 acquisition was on the 31 August, meaning that the interferogram contains 7 days of postseismic displacement in addition to the coseismic signal. We use GPS displacements calculated between the day before the earthquake and the 31 August, for continuity between the two data sets.

Spatiotemporal variation in propagation path properties through the atmosphere adds noise to InSAR scenes that is spatially correlated. To account for the covariance of this noise we calculate the variance-covariance matrix by selecting an undeforming region of the interferogram and computing the 1-D semivariogram (e.g., Lohman & Simons, 2005; Oliver & Webster, 2014), which is a function of variance with distance that describes the spatial dependence in a data set (Foody & Atkinson, 2002). This model gives us three values: the sill, nugget, and range, which are indicated on our semivariogram shown in supporting information Figure S16 and that can be used to estimate the spatially correlated error in the InSAR data. The nugget indicates the level of spatially independent noise present, and the sill is the maximum value of the semivariance as the range tends to infinity (Foody & Atkinson, 2002). The range is the distance at which the semivariance reaches approximately 95% of the sill (Curran, 1988) and is the distance over which we expect data points to be spatially correlated. We calculate a sill of 5×10^{-4} m^2, nugget of 1×10^{-5} m^2, and a range of 12.8 km from the semivariogram, which we use to calculate the variance-covariance matrix using the exponential function:

$$\mathbf{\Sigma_d} = (\text{sill-nugget}) \times e^{\frac{-3x}{r}} \tag{12}$$

where x is the distance between each InSAR data point, r is the range, and $\mathbf{\Sigma_d}$ has dimensions $N \times N$ where N is the number of data points. At $r = 0$ the variance of a data point is equal to the sill.

A larger range would mean that covariance between data points extends over a larger distance (e.g., larger wavelength atmospheric signals). A larger sill would mean a higher variance for individual data points (at $r = 0$), that is, greater uncertainty on individual data points and also higher covariance between data points. A larger nugget indicates decreased covariance if the sill remains the same. Many studies find the range for an interferogram to be >10 km, the standard deviation ($\sqrt{\text{variance}}$) of the sill to be a couple of centimeters and the nugget to be significantly smaller than the sill (e.g., Bekaert et al., 2016; Hanssen, 2010). The values we estimate for these parameters are indeed in accordance with these previous studies.

Table 1
Details of the Fault Geometry

Strike	Dip	Rake	Center (UTM *x*)	Center (UTM *y*)	Length (km)	Top depth (km)	Bottom depth (km)
337	90	180	559561	4232632	6.88	0	13
343	90	180	557784	4237229	2.99	0	13
4	90	180	557434	4239865	2.42	0	13
337	90	180	557850	4240305	9.45	0	13

Note. The first three lines are one fault (southwestern fault) modeled as three separate rectangles to capture the curve in the fault geometry, and the forth line is a separate fault segment (northeastern fault). The center refers to the updip surface projection of the fault and the UTM zone is 10S. This fault setup can be seen in Figure 7.

4.2. Model Parameters

We constrained the surface fault using the rupture map of Hudnut et al. (2014). Based on this we modeled the fault as two vertical strands, one with three sections to capture the fault curve and one straight (details given in Table 1). We assumed slip correlation did not continue between the two separate fault strands.

Correlation lengths for the two faults were calculated based upon the length and width of the faults using equations (4) and (5), giving the correlation downdip as $a_{dd} = 5,330$ m and along-strike as $a_{as} = 5,070$ m for the northeastern fault strand and $a_{dd} = 5,330$ m and $a_{as} = 6,040$ m for the separate segments on the most southwestern fault strand. We note that ideally these parameters would be drawn from their prior distributions, discussed more in section 5.4. The Lamé parameters used in the Okada Green's function calculation were $\lambda = \mu = 3.23$ GPa. The initial probability target (later used in sensitivity tests to adjust step sizes) was 10^{-4}.

The InSAR and GPS data were only weighted according to their variance-covariance. In this case an offset and ramp has been removed from the InSAR before the inversion.

To ensure the inversion had reached convergence we check four criteria:

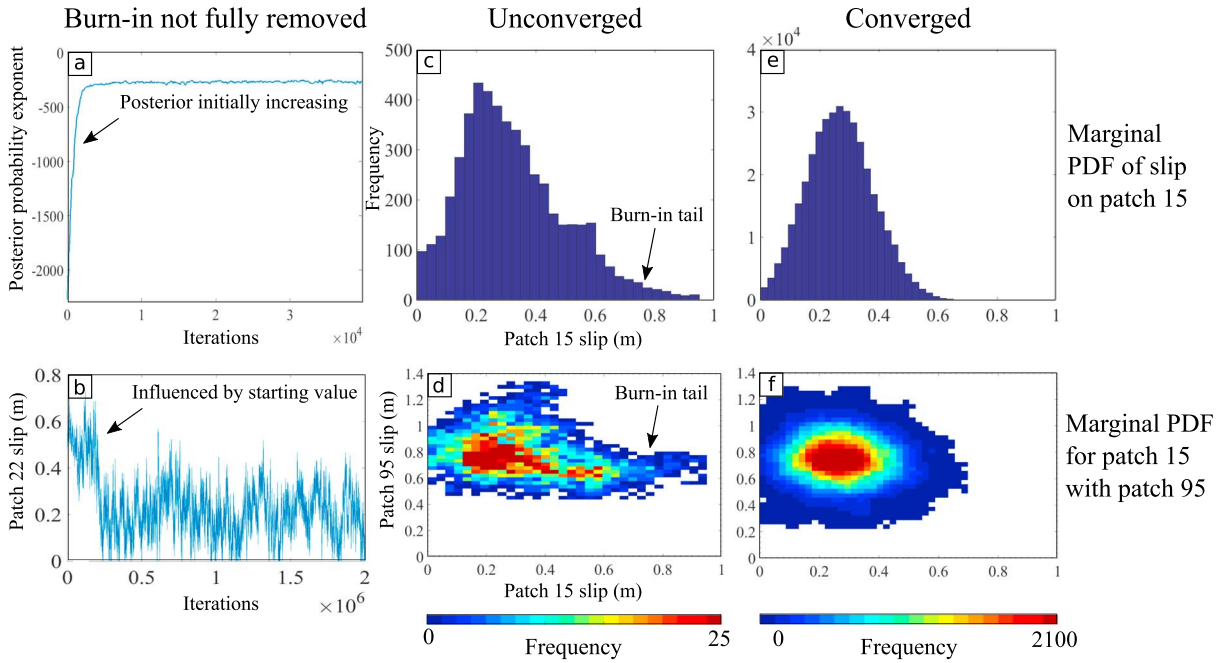

Figure 6. Illustrating converged and unconverged solutions and those with the burn-in not fully removed. Panels a and b show the posterior probability and value of one of the model slips on fault patch 22, respectively; in this case they are both still influenced by the starting parameters because some of the burn-in remains. Note the difference in *x* axis between a and b, because we have zoomed in on a for clarity. Panels c and d show unconverged inversion: the PDF is not filled out, and the joint PDF is rough. In this example we have also left the burn-in present, which is shown by an elongate tail extending from the starting value of ~0.9 m. Panels e and f show converged solutions of c and d: Both PDFs are smooth. Note that the frequency shown by the color bar for the joint PDFs is not plotted on the same scale, to illustrate how the PDF would look at the end of the unconverged inversion, rather than in comparison to the later one.

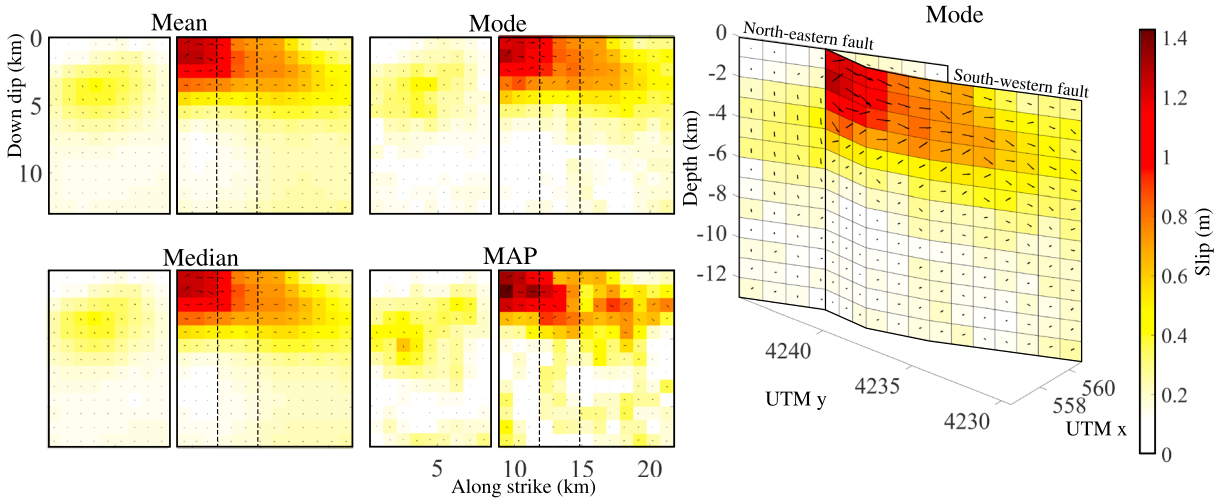

Figure 7. Results of inversion for the Napa Valley earthquake incorporating a von Karman prior. All five show the same fault plane, which is in two strands, and dotted vertical lines indicate the bends on the southwestern fault. The first three are different statistical parameters to visually capture the full probability density function, whereas the 'MAP' solution is the saved trial with the maximum a posteriori (MAP) result. Peak slip is around ~1.2 m and at a depth of 2 km. The right-hand figure shows the mode solution shown in 3-D, showing the fault geometry of the two separate strands more clearly. UTM = universal time meridian.

1. Smoothness of histograms for each model parameter;
2. Smoothness of 2-D histograms of the six patches with the most slip;
3. Posterior probability is no longer increasing;
4. The value of each parameter through the inversion has reached stability and does not have an increasing or decreasing trend.

As standard we remove the first 2,000 saved trials to remove the burn-in. We then check if the posterior probability is stable and the form of the joint PDFs. An increase in the posterior probability for the first saved trials or a visible tail in the joint PDFs implies that the burn-in has not been fully removed, and we increase the burn-in period so as to remove these two effects.

Examples of unconverged and converged solutions with burn-in present are shown in Figure 6.

4.2.1. Priors

For the slip prior we used a uniform probability density between 0 and 50 m. The upper bound slip prior was set arbitrarily high, but we found that slip at no point explored values higher than 1.8 m, so this choice of high upper bound made no difference to the efficiency of our inversion. For rake we used a uniform probability density between 135° and 225° on the southwestern fault and 135° and 270° on the northeastern fault where previous studies have found normal motion on a releasing step over of the S. Napa fault (Floyd et al., 2016). The probability outside of the ranges given for slip and rake is 0, so model parameters were only drawn from within these ranges. We used a logarithmic prior for α as discussed in section 2.3.

4.3. Napa von Karman Results

As discussed previously, the solution of a Bayesian inversion is a multidimensional PDF, which is difficult to visualize, so we have included a video showing a selection of the saved results (supporting information Video S29). To illustrate this with static images we have used statistical parameters estimated from the model parameters' PDFs. These are shown in Figure 7, for a Bayesian inversion with von Karman smoothing. The "mode" for each patch is shown in 3-D to show fault geometry and, as for the synthetic tests, we calculate the joint slip mode and rake mode for each patch by finding the value of the peak of the highest bar in the 2-D histogram of slip against rake. The mode, mean, and median have not been drawn as trials, but by plotting them all we hope to give an indication of where slip is most probable and the probable direction of rake. The maximum a posteriori (MAP) solution is the multidimensional mode solution: the single saved solution that maximizes the posterior probability density function (i.e., that maximizes both the prior and the likelihood).

These results show that the majority of slip occurred as strike-slip motion on the southwestern fault, near to the surface. We found peak magnitude of slip of ~1.2 m at about 2-km depth. This is similar in magnitude

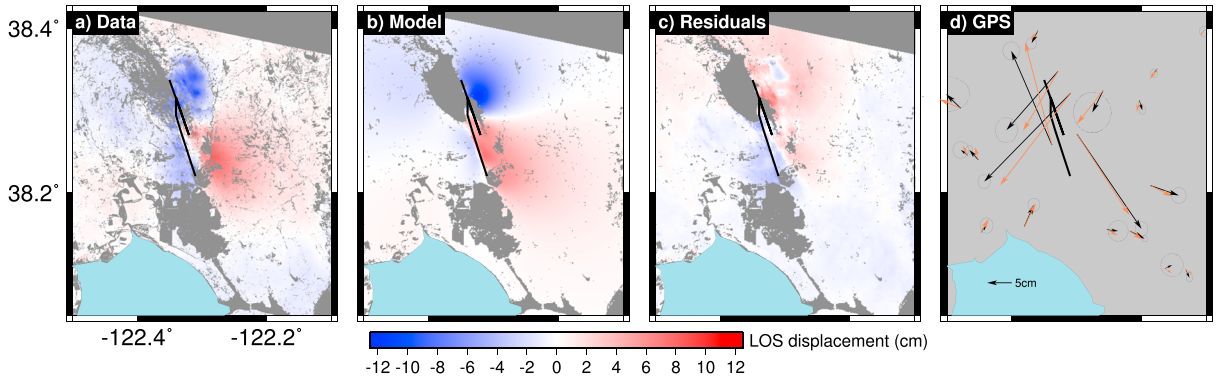

Figure 8. The InSAR data (a), model fit (b), and residuals (c) for the von Karman regularized MAP slip solution on selected patches for the Napa earthquake. Panel d shows the closest GPS data (black) to the fault, with model vector (orange) and 95% confidence intervals. LOS = line of sight.

and location to InSAR and GPS studies by Guangcai et al. (2015), Wei et al. (2015), and Floyd et al. (2016) and the strong motion study by Zhang, Wang, et al. (2015). Many studies also find a peak magnitude of 1.2 m, though find slip deeper at ~5 km (Barnhart et al., 2015; Dreger et al., 2015; Melgar et al., 2015). On the northeastern fault there was a component of normal motion between 3 and 6 km depth, as also found by Wei et al. (2015) and Floyd et al. (2016).

The MAP result gives a moment of 2.78×10^{18} Nm which is higher than the seismic moment of 1.33×10^{18} Nm from the USGS event page. Part of this overestimation of the energy release may be due to the 7-day afterslip included in the InSAR and GPS.

Figure 8 shows the fit of the MAP model to the InSAR and GPS data. The predicted InSAR displacements fit the magnitude and wavelength of the signals in the data, but there are some areas of high residuals. The InSAR misfit on the eastern side of the southwestern fault is in part due to displacements on a separate third fault, which ruptured at the surface in this earthquake but which we have not modeled here (Hudnut et al., 2014). The three GPS points nearest to the fault are not fit within the 95% error ellipses and show a very similar misfit as found by Floyd et al. (2016) using the same data. The complexity of surface deformation in the north-east, where two GPS points are poorly fit, is shown in the InSAR data (panel a of Figure 8). This could be due to an unmodeled fault as suggested by Guangcai et al. (2015) or due to local surface effects and changes in elastic properties in the north-east due to a change in lithology to Quaternary sediments. The modeling of these complexities is beyond the scope of this paper.

5. Discussion

5.1. Comparison of VK and Laplacian Result for Napa

For comparison we also solved for slip in a Bayesian fashion using a Laplacian prior, in which we solved simultaneously for the model fit to the data and for the fit of the model to a Laplacian distribution as well as for the Laplacian smoothing hyperparameter. The results of the mode solutions are shown in Figure 9 and fit to the data for the Laplacian solution is shown in supporting information Figure S17. Both put more slip on the southwestern fault (shown on the right in Figure 9) than the northeastern fault and find a peak slip of just over 1 m; however, the Laplacian solution has a slightly higher peak slip and extends this slip further along the southwestern fault. The standard deviation on the southwestern fault is significantly larger than for the von Karman regularized inversion, showing the larger uncertainty for the Laplacian solution in this area. This is not unexpected as the von Karman prior provides a tighter constraint than the Laplacian prior, but it is an important result, as the tighter constraint is based upon observed features of fault slip. The von Karman solution puts a slightly lower magnitude of slip on the northeastern fault and fits the data better in this region (supporting information Figure S17).

The moment of the MAP Laplacian solution is 2.87×10^{18} Nm, which is significantly larger than the USGS moment of 1.33×10^{18} Nm, and slightly larger than the von Karman MAP moment of 2.78×10^{18} Nm.

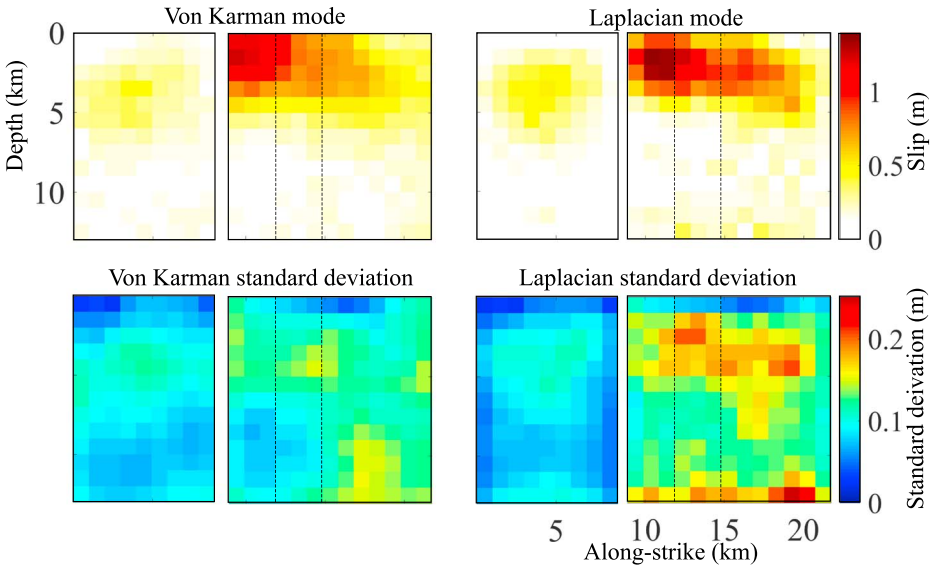

Figure 9. Results (mode) of a Bayesian inversion incorporating von Karman (left) and Laplacian (right) priors. Below, the standard deviation of each fault patch. The results are broadly similar in magnitude but vary in location, as the Laplacian extends slip along strike for the southwestern fault (shown on the right) and puts higher slip on the northeastern fault. The uncertainties are much higher for the Laplacian solution, as is evident from the higher standard deviations across the fault. For comparison the slip magnitude color bar is the same as Figure 7.

We find that the von Karman solution extends high slip right to the surface, in contrast with the Laplacian solution and many other geodetic studies for this earthquake (Barnhart et al., 2015; Floyd et al., 2016; Guangcai et al., 2015; Melgar et al., 2015; Wei et al., 2015). Oversmoothing, as well as nonnegativity in the inversion and lack of data near the fault have been found to result in a lack of slip at the surface and apparent shallow-slip deficit (Xu et al., 2016). By solving for the degree of smoothing with the hyperparameter α^2 we speculate that the von Karman regularization could potentially resolve slip at the surface better in the Napa Valley earthquake. However, we note that it is hard to directly compare specifics of slip solutions between published studies since different studies use different fault geometry, including one fault (Barnhart et al., 2015; Dreger et al., 2015; Melgar et al., 2015; Zhang, Wang, et al., 2015), two straight faults (Wei et al., 2015; Ji et al., 2015), or a more complicated curved fault geometry such as we used here (Floyd et al., 2016; Guangcai et al., 2015).

These two different results show the bias that a regularization technique can cause.

5.2. Trade-offs

We examined trade-offs between different model parameters for the von Karman solution. First we computed the correlation coefficients between all the model parameters, using their full posterior PDFs (supporting information Figure S18). This identified some interesting behavior which we explored further by examining the individual histograms. We find strong positive trade-offs between the five patches with the largest magnitude of slip. This is as expected because they are located close together, at distances smaller than the von Karman correlation lengths (supporting information Figure S19). We also examined the spatial distribution of slip and potential correlations. We found that there is no covariance between the patches with the highest slip on the south-western fault and patches with the highest slip on the north-eastern fault as shown in the supporting information Figure S20. We also found no covariance between the patches with maximum slip on the southwestern fault and patches along-strike from them (supporting information Figure S21). There is positive correlation between the magnitude of slip of patches downdip from each other on the northeastern fault (supporting information Figure S22), though not on patches farthest away from each other, indicating that this is largely due to the von Karman correlation.

The von Karman correlation acts on the magnitude of slip but it does not act upon the rake. We found that normal faulting sense of motion was required on the northeastern fault to fit the InSAR in this area. In light of this, we consider the trade-offs between the normal-faulting sense of motion rake on this fault. We found that near the surface, the rake was well constrained to have normal faulting motion, up to the maximum of the rake prior, 270° (supporting information Figure S23). At depth the rake is very poorly constrained and all

of parameter space within the rake prior is almost equally searched. On the southwestern fault we observed some oscillatory slip along-strike; the histograms in supporting information Figure S24 show that many patches display either no correlation or negative correlation with the rake of a patch next to them but show either no correlation or positive correlation with a patch two along. This indicates that patches next to each other are anticorrelated, and so we observe an oscillation in rake along the fault.

From our trade-off analysis, the main influence on magnitude of slip magnitude for any given patch is that of its nearest neighbors, as is to be expected from von Karman regularization. Rake shows some oscillatory behavior, with the rake of a patch likely to be anticorrelated to the rake of its immediate neighbors along-strike and positively correlated to the rake on those patches that are separated along-strike by a single patch.

5.3. Slip at the Step Over

Our fault geometry includes a step over, with the rupture originating at the hypocenter at 11-km depth on the southwestern fault and propagating to the northwest (Wei et al., 2015). Strike-slip earthquakes have often been found to stop at such step overs (Wesnousky, 2006), and how earthquake rupture is able to propagate through complicated geometry and across step overs like these is important in understanding why earthquake ruptures stop and subsequently for seismic hazard. We investigated the trade-offs at the overlap area of the two faults. The faults overlap by over 5 km but are separated by approximately 1.5 km at the maximum separation, which is in keeping with observations of overlap and separation for echelon strike-slip faults, which are themselves self-similar (Aydin & Schultz, 1990). We impose von Karman regularization separately on the two faults, so any form of correlation is independent of regularization. We find that there is a negative correlation between the two fault strands: where there is high slip on the southwestern fault, there is low slip on the northeastern strand (supporting information Figure S25). There is also a change in rake, with the southwestern fault undergoing primarily right-lateral slip motion, whereas the northeastern fault displays largely normal fault motion, which is required to fit the InSAR to the north-east of the surface rupture.

This negative correlation means that there is a sharp drop in slip from one fault to the other. Observations of slip magnitude at step overs suggests that an abrupt decrease in slip magnitude at the step over makes the rupture more likely to continue to rupture on the other side (Elliott et al., 2009), as does the proximity of two faults (Wesnousky, 2006), both of which we observe in this study. This proximity also means that stress may increase or decrease on one fault due to failure of the other, made more complicated by their overlap and curved geometry of the southwestern fault. This interaction between the faults affects how fault systems grow (Cowie, 1998) and simplify over time (Wesnousky, 1988). The significantly lower slip on the northeastern fault may suggest that while the rupture was able to cross this geometrical complexity, the earthquake rupture may have been impeded by it, as has frequently been documented and modeled at step overs (Harris & Day, 1993; Wesnousky, 1988).

We note that this interpretation is affected by our assumption to treat the two faults as independent and not smooth between them. We have also assumed that they remain as separate faults at depth and do not merge.

5.4. Fault Parameterization—Fault Size

In contrast to the Laplacian smoothness constraint, the von Karman constraint penalizes regions of zero slip. If the modeled fault plane is larger than the area that actually slipped, a Laplacian smoothed solution would give a high probability to zero slip in regions that are not well resolved, whereas the von Karman correlation would give greater probability to nonzero slip in these areas. This is because regions of zero slip have 100% correlation at all distances, which is inconsistent with a VK distribution. This is particularly a problem at depth or when lack of data mean resolution is poor elsewhere. Ideally, only areas that actually slipped should be included in a von Karman constrained inversion.

Additionally, choice of fault dimensions in a von Karman slip inversion affects the correlation lengths (empirical equations (4) and (5) include fault length and width). In the case of the Napa Valley earthquake we could constrain the fault geometry due to an abundance of mapped surface ruptures (Hudnut et al., 2014), but if a rupture does not break the surface then some constraint on length must be adopted, such as the distribution of aftershocks. Any vastly incorrect estimation of fault length and therefore correlation parameters at this initial stage has the potential to bias the results of the inversion.

The correlation lengths themselves are empirical scaling relations with their own uncertainty for any particular fault size, and so ideally, these would be drawn from their prior distribution, as discussed in Mai and Beroza (2002).

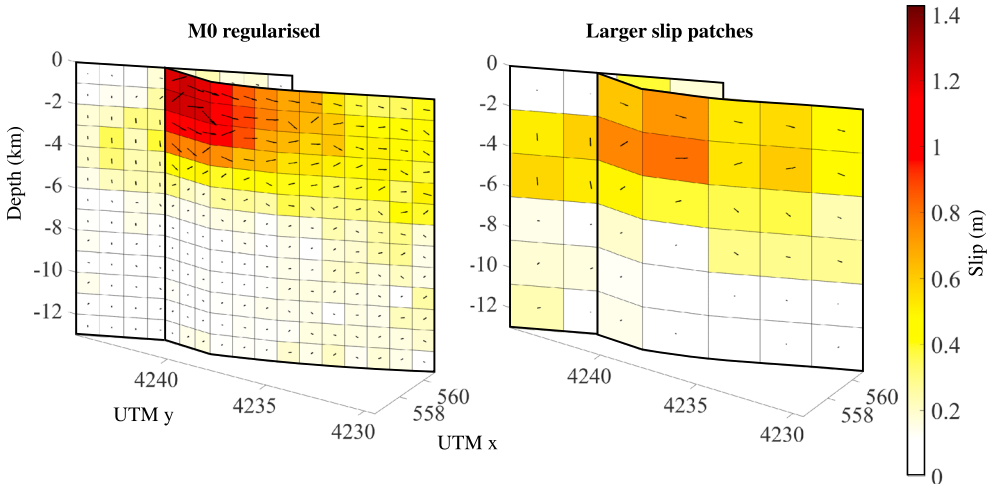

Figure 10. The mode results of Bayesian inversions for the Napa earthquake using von Karman regularization and moment regularization (left) or bigger slip patches (right). For direct comparison the scale bar is the same as Figure 7. UTM = universal time meridian.

Solving for fault length and correlation parameters during the inversion would solve these issues. This would mean that throughout an MCMC chain the size of the fault would increase or decrease in length and width and correlation parameters would be drawn from a normal distribution, centered on the value for the current length and width. This would require recalculating the correlation matrix, $\mathbf{\Sigma_s}$, which adds computational expense, and solving for fault size this would transform the inversion into a transdimensional problem (e.g., Dettmer et al., 2014). We leave the implementation of this to future work.

5.5. Fault Parameterization—Number of Slip Patches

In this paper we have chosen the slip patches to be approximately 1 km × 1 km in size. In the literature there is very little consistency in choosing the number or dimension of these patches, and they range from being less than 1 km in length up to greater than 25 km, rectangular or triangular, with up to thousands of patches. The choice of patch size should be based on model resolving power (e.g., Page et al., 2009) as determined by the data and, particularly for Bayesian inversions, computational expense.

If a fault is divided into more patches than can be resolved by the data, this model will give an artificial level of detail. But if too few patches are used on a fault, then the data will be poorly fit and the model unrepresentative.

In order to correctly parameterize the model, methods include determining the size of the patches to reflect the resolving power of surface displacements (Atzori & Antonioli, 2011; Barnhart & Lohman, 2010) before commencing an inversion. Other methods include using self-adapting grids that change patch size and number throughout the inversion (Dettmer et al., 2014).

As a simple test to compare the effect of the number of slip patches, we solved for the Napa earthquake using exactly the same inversion parameters as the von Karman inversion above, but with each patch twice as long and twice as wide. Figure 10 shows that the solution has a similar location of peak slip as the von Karman inversion with smaller patches but the moment is 2.77×10^{18} Nm, which is also significantly bigger than the USGS moment of 1.33×10^{18} Nm but roughly the same as the von Karman regularized solution with smaller patches.

We also solve for von Karman regularization across the entire fault with moment regularization, using a Gaussian prior with a mean of the USGS moment of 1.33×10^{18} Nm and a standard deviation of 1.07×10^{17}. Here we found the MAP result gives a moment of 2.43×10^{18} Nm, which is still significantly larger than the USGS moment of 1.33×10^{18} Nm, though closer to the USGS value than the von Karman regularization with smaller slip patches. Other geodetic studies also found moments larger than the USGS moment; the study by Guangcai et al. (2015) found a value of 2.07×10^{18}, and the study by Floyd et al. (2016) found a value of 1.67×10^{18}. Some of this difference to the USGS moment may be due to the documented differences

between geodetic and seismically derived moment (Weston et al., 2011), as well as to the 7 days of postseismic deformation present in the InSAR and GPS data (e.g., Floyd et al., 2016).

5.6. Solving for Smoothing Parameters

The von Karman distribution is determined by three parameters: the Hurst parameter and along-strike and downdip correlation coefficients. Here we have used the average value for strike slip faults determined by Mai and Beroza (2002) rather than solving for them and for the synthetic tests have used the same correlation lengths for generating the input slip distributions and for the inversion. An incorrect assumption of correlation lengths is likely to bias model results, and in future work, to be as objective as possible, we propose to solve for them as hyperparameters with priors constrained by the full distribution determined by Mai and Beroza (2002).

There is evidence that faults become smoother with increasing slip (Brodsky et al., 2011; Sagy et al., 2007) due to fault maturity. This can be characterized using the Hurst parameter, which has been carried out for several exhumed fault surfaces (Bistacchi et al., 2011; Candela et al., 2011, 2012). Prior knowledge of the Hurst parameter or the degree of maturity of a particular fault could therefore help constrain the Hurst parameter in slip inversions better. Alternatively, solving for correlation coefficients and the Hurst parameter within the slip inversion could be used to estimate the smoothness of active faults are and consequently their maturity. This could be tested on faults of known age.

6. Conclusion

In light of all the evidence that earthquake slip shows fractal properties we suggest that von Karman regularization should be the default for slip inversions in the future. Our tests show that even if the underlying slip were not fractal, von Karman regularization does at least as well as the commonly used Laplacian regularization. We have developed a method to solve for earthquake slip inversion in a Bayesian sense, with the capability of incorporating von Karman, Laplacian, or no smoothing and with the potential to add other spatial constraints in the future. MCMC models are more computationally expensive than some other inversion algorithms but enable us to fully capture the plethora of model solutions that fit the prior and data and characterize the uncertainties and trade-offs between parameters. We have made the search more efficient by using two steps in the MCMC chain and adapting parameter step size as the inversion proceeds. We find that a Laplacian-smoothed inversion places slip in different locations to von Karman regularization for the Napa Valley earthquake, and the von Karman solution gives much tighter confidence bounds on slip. We argue that this tighter confidence represents an important improvement on the solution, since the tighter constraint arises from the self-affine prior we are imposing, which is based on observational evidence. We therefore suggest that von Karman regularization is a better constraint since it is capable of capturing the self-affine properties of coseismic slip.

Acknowledgments

This work was supported by the UK Natural Environment Research Council (NERC) through the Leeds-York NERC Doctoral Training Program (NE/L002574/1) and COMET, the NERC Centre for Observation and Modelling of Earthquakes, Volcanoes and Tectonics. Some figures were prepared using the public domain GMT software (Wessel & Smith, 1991). We are grateful to Tim Wright, Jessica Hawthorne, Laura Gregory, and Tom Ingleby for useful discussions, as well as to Martin Mai, two anonymous reviewers, Editor Yehuda Ben-Zion, and Associate Editor Yoshihiro Kaneko for their helpful and constructive reviews that greatly improved this manuscript. Data used for the synthetic tests are available in the supporting information, and for InSAR and GPS data from the Napa earthquake please contact authors.

References

Atzori, S., & Antonioli, A. (2011). Optimal fault resolution in geodetic inversion of coseismic data. *Geophysical Journal International*, *185*(1), 529–538. https://doi.org/10.1111/j.1365-246X.2011.04955.x

Aviles, C. A., Scholz, C. H., & Boatwright, J. (1987). Fractal analysis applied to characteristic segments of the San Andreas Fault. *Journal of Geophysical Research*, *92*(B1), 331–344. https://doi.org/10.1029/JB092iB01p00331

Avouac, J.-P., Meng, L., Wei, S., Wang, T., & Ampuero, J.-P. (2015). Lower edge of locked Main Himalayan Thrust unzipped by the 2015 Gorkha earthquake. *Nature Geoscience*, *8*(9), 708–711. https://doi.org/10.1038/ngeo2518

Aydin, A., & Schultz, R. (1990). Effect of mechanical interaction on the development of strike-slip faults with echelon patterns. *Journal of Structural Geology*, *12*(1), 123–129. https://doi.org/10.1016/0191-8141(90)90053-2

Barnhart, W. D., & Lohman, R. B. (2010). Automated fault model discretization for inversions for coseismic slip distributions. *Journal of Geophysical Research*, *115*, B10419. https://doi.org/10.1029/2010JB007545

Barnhart, W. D., Murray, J. R., Yun, S., Svarc, J. L., Samsonov, S. V., Fielding, E. J., et al. (2015). Geodetic constraints on the 2014 M 6.0 South Napa earthquake. *Seismological Research Letters*, *86*(2), 335–343. https://doi.org/10.1785/0220140210

Bekaert, D. P. S., Segall, P., Wright, T. J., & Hooper, A. J. (2016). A network inversion filter combining GNSS and InSAR for tectonic slip modeling. *Journal of Geophysical Research: Solid Earth*, *121*, 2069–2086. https://doi.org/10.1002/2015JB012638

Ben-Zion, Y. (2008). Collective behavior of earthquakes and faults: Continuum-discrete transitions, progressive evolutionary changes, and different dynamic regimes. *Reviews of Geophysics*, *46*, RG4006. https://doi.org/10.1029/2008RG000260

Bistacchi, A., Griffith, W. A., Smith, S. A. F., Di Toro, G., Jones, R., & Nielsen, S. (2011). Fault roughness at seismogenic depths from LIDAR and photogrammetric analysis. *Pure and Applied Geophysics*, *168*(12), 2345–2363. https://doi.org/10.1007/s00024-011-0301-7

Brodsky, E. E., Gilchrist, J. J., Sagy, A., & Collettini, C. (2011). Faults smooth gradually as a function of slip. https://doi.org/10.1016/j.epsl.2010.12.010

Brown, S. R., & Scholz, C. H. (1985). Broad bandwidth study of the topography of natural rock surfaces. *Journal of Geophysical Research*, *90*(B14), 12,575–12,582. https://doi.org/10.1029/JB090iB14p12575

Bruhat, L., Fang, Z., & Dunham, E. M. (2016). Rupture complexity and the supershear transition on rough faults. *Journal of Geophysical Research: Solid Earth*, *121*, 210–224. https://doi.org/10.1002/2015JB012512

Campbell, G. E., Walker, R. T., Abdrakhmatov, K., Jackson, J., Elliott, J. R., Mackenzie, D., et al. (2015). Great earthquakes in low-strain-rate continental interiors: An example from SE Kazakhstan. *Journal of Geophysical Research: Solid Earth*, *120*, 5507–5534. https://doi.org/10.1002/2015JB011925

Candela, T., Renard, F., Bouchon, M., Schmittbuhl, J., & Brodsky, E. E. (2011). Stress drop during earthquakes: Effect of fault roughness scaling. *Bulletin of the Seismological Society of America*, *101*(5), 2369–2387. https://doi.org/10.1785/0120100298

Candela, T., Renard, F., Klinger, Y., Mair, K., Schmittbuhl, J., & Brodsky, E. E. (2012). Roughness of fault surfaces over nine decades of length scales. *Journal of Geophysical Research*, *117*, B08409. https://doi.org/10.1029/2011JB009041

Cowie, P. A. (1998). A healing-reloading feedback control on the growth rate of seismogenic faults. *Journal of Structural Geology*, *20*(8), 1075–1087. https://doi.org/10.1016/S0191-8141(98)00034-0

Curran, P. (1988). The semivariogram in remote sensing: An introduction. *Remote Sensing of Environment*, *24*(3), 493–507. https://doi.org/10.1016/0034-4257(88)90021-1

Dettmer, J., Benavente, R., Cummins, P. R., & Sambridge, M. (2014). Trans-dimensional finite-fault inversion. *GJI Seismology*, *199*, 735–751. https://doi.org/10.1093/gji/ggu280

Dolan, S., Bean, C., & Riollet, B. (1998). The broad-band fractal nature of heterogeneity in the upper crust from petrophysical logs. *Geophysical Journal International*, *132*(3), 489–507. https://doi.org/0.1046/j.1365-246X.1998.00410.x

Dreger, D. S., Huang, M.-H., Rodgers, A., Taira, T., & Wooddell, K. (2015). Kinematic finite-source model for the 24 August 2014 South Napa, California, earthquake from joint inversion of seismic, GPS, and InSAR data. *Seismological Research Letters*, *86*(2A), 327–334. https://doi.org/10.1785/0220140244

Elliott, A. J., Dolan, J. F., & Oglesby, D. D. (2009). Evidence from coseismic slip gradients for dynamic control on rupture propagation and arrest through stepovers. *Journal of Geophysical Research*, *114*, B02313. https://doi.org/10.1029/2008JB005969

Elliott, J. R., Elliott, A. J., Hooper, A. J., Larsen, Y., Marinkovic, P., & Wright, T. J. (2015). Earthquake monitoring gets boost from new satellite. *EOS*, *96*. https://doi.org/10.1029/2015EO023967

Evans, E. L., & Meade, B. J. (2012). Geodetic imaging of coseismic slip and postseismic afterslip: Sparsity promoting methods applied to the great Tohoku earthquake. *Geophysical Research Letters*, *39*, L11314. https://doi.org/10.1029/2012GL051990

Fang, Z., & Dunham, E. M. (2013). Additional shear resistance from fault roughness and stress levels on geometrically complex faults. *Journal of Geophysical Research: Solid Earth*, *118*, 3642–3654. https://doi.org/10.1002/jgrb.50262

Fisher, D. S., Dahmen, K., Ramanathan, S., & Ben-Zion, Y. (1997). Statistics of earthquakes in simple models of heterogeneous faults. *Physical Review Letters*, *78*(25), 4885–4888. https://doi.org/10.1103/PhysRevLett.78.4885

Floyd, M. A., Walters, R. J., Elliott, J. R., Funning, G. J., Svarc, J. L., Murray, J. R., et al. (2016). Spatial variations in fault friction related to lithology from rupture and afterslip of the 2014 South Napa, California, earthquake. *Geophysical Research Letters*, *43*, 6808–6816. https://doi.org/10.1002/2016GL069428

Foody, G., & Atkinson, M. (2002). *Uncertainty in remote sensing and GIS* (pp. 100–101). Chichester: John Wiley.

Fukuda, J., & Johnson, K. M. (2008). A fully Bayesian inversion for spatial distribution of fault slip with objective smoothing. *Bulletin of the Seismological Society of America*, *98*(3), 1128–1146. https://doi.org/10.1785/0120070194

Funning, G. J., Barke, R. M., Lamb, S. H., Minaya, E., Parsons, B., & Wright, T. J. (2005). The 1998 Aiquile, Bolivia earthquake: A seismically active fault revealed with InSAR. *Earth and Planetary Science Letters*, *232*(1-2), 39–49. https://doi.org/10.1016/j.epsl.2005.01.013

Guangcai, F., Zhiwei, L., Xinjian, S., Bing, X., & Yanan, D. (2015). Source parameters of the 2014 Mw 6.1 South Napa earthquake estimated from the Sentinel 1A, COSMO-SkyMed and GPS data. *Tectonophysics*, *655*, 139–146. https://doi.org/10.1016/j.tecto.2015.05.018

Gutenberg, B., & Richter, C. F. (1955). Magnitude and energy of earthquakes. *Nature*, *176*, 795. https://doi.org/10.1038/176795a0

Hanssen, R. F. (2010). *Radar interferometry: Data interpretation and error analysis* (pp. 140–141). New york: Kluwer Academic.

Harris, R. A., & Day, S. M. (1993). Dynamics of fault interaction: Parallel strike-slip faults. *Journal of Geophysical Research*, *98*(B3), 4461–4472. https://doi.org/10.1029/92JB02272

Harris, R. A., & Segall, P. (1987). Detection of a locked zone at depth on the Parkfield, California, segment of the San Andreas Fault. *Journal of Geophysical Research*, *92*(B8), 7945. https://doi.org/10.1029/JB092iB08p07945

Hooper, A. J. (2012). Earthquake slip distribution estimation, using a random vector approach. In *AGU Fall Meeting Abstracts*. -1, 08.

Hooper, A. J., Pietrzak, J., Simons, W., Cui, H., Riva, R., Naeije, M., et al. (2013). Importance of horizontal seafloor motion on tsunami height for the 2011 Mw=9.0 Tohoku-Oki earthquake. *Earth and Planetary Science Letters*, *361*, 469–479. https://doi.org/10.1016/j.epsl.2012.11.013

Hudnut, K., Brocher, T., Prentice, C., Boatwright, J., Brooks, B., Aagaard, B. T., et al. (2014). Key recovery factors for the August 24, 2014, South Napa Earthquake, Tech. rep., U.S. Geological Survey Open-File Report 2014-1249. https://doi.org/2331-1258 (online)

Ji, C., Archuleta, R. J., & Twardzik, C. (2015). Rupture history of 2014 M_w 6.0 South Napa earthquake inferred from near-fault strong motion data and its impact to the practice of ground strong motion prediction. *Geophysical Research Letters*, *42*, 2149–2156. https://doi.org/10.1002/2015GL063335

Jolivet, R., Duputel, Z., Riel, B., Simons, M., Rivera, L., Minson, S. E., et al. (2014). The 2013 Mw 7.7 Balochistan Earthquake: Seismic potential of an accretionary wedge. *Bulletin of the Seismological Society of America*, *104*(2), 1020–1030. https://doi.org/10.1785/0120130313

Kanamori, H., & Anderson, D. L. (1975). Theoretical basis of some empirical relations in seismology. *Bulletin of the Seismological Society of America*, *65*(5), 1073–1095.

Lindsey, E. O., & Fialko, Y. (2016). Geodetic constraints on frictional properties and earthquake hazard in the Imperial Valley, Southern California. *Journal of Geophysical Research: Solid Earth*, *121*, 1097–1113. https://doi.org/10.1002/2015JB012516

Lohman, R. B., & Simons, M. (2005). Some thoughts on the use of InSAR data to constrain models of surface deformation: Noise structure and data downsampling. *Geochemistry, Geophysics, Geosystems*, *6*, Q01007. https://doi.org/10.1029/2004GC000841

Lorito, S., Romano, F., Atzori, S., Tong, X., Avallone, A., McCloskey, J., et al. (2011). Limited overlap between the seismic gap and coseismic slip of the great 2010 Chile earthquake. *Nature Geoscience*, *4*(3), 173–177. https://doi.org/10.1038/ngeo1073

Mai, P. M., & Beroza, G. C. (2002). A spatial random field model to characterize complexity in earthquake slip. *Journal of Geophysical Research*, *107*(B11), 2308. https://doi.org/10.1029/2001JB000588

Mai, P. M., Galis, M., Thingbaijam, K. K. S., Vyas, J. C., & Dunham, E. M. (2017). Accounting for fault roughness in pseudo-dynamic ground-motion simulations. *Pure and Applied Geophysics*, *174*(9), 3419–3450. https://doi.org/10.1007/s00024-017-1536-8

Mai, P. M., Schorlemmer, D., Page, M., Ampuero, J., Asano, K., Causse, M., et al. (2016). The Earthquake-Source Inversion Validation (SIV) Project. *Seismological Research Letters*, *87*(3), 690–708. https://doi.org/10.1785/0220150231

Mandelbrot, B. B. (1983). The fractal geometry of nature, Freeman.

Melgar, D., Geng, J., Crowell, B. W., Haase, J. S., Bock, Y., Hammond, W. C., & Allen, R. M. (2015). Seismogeodesy of the 2014 M_w 6.1 Napa earthquake, California: Rapid response and modeling of fast rupture on a dipping strike-slip fault. *Journal of Geophysical Research: Solid Earth*, *120*, 5012–5033. https://doi.org/10.1002/2015JB011921

Milliner, C. W., Dolan, J. F., Hollingsworth, J., Leprince, S., Ayoub, F., & Sammis, C. (2015). Quantifying near-field and off-fault deformation patterns of the 1992 M_W 7.3 Landers earthquake. *Geochemistry, Geophysics, Geosystems*, *16*, 1525–2027. https://doi.org/10.1002/2014GC005693

Milliner, C. W. D., Sammis, C., Allam, A. A., Dolan, J. F., Hollingsworth, J., Leprince, S., & Ayoub, F. (2016). Resolving fine-scale heterogeneity of co-seismic slip and the relation to fault structure. *Scientific Reports*, *6*, 27201. https://doi.org/10.1038/srep27201

Minson, S. E., Simons, M., & Beck, J. L. (2013). Bayesian inversion for finite fault earthquake source models I—Theory and algorithm. *Geophysical Journal International*, *194*(3), 1701–1726. https://doi.org/10.1093/gji/ggt180

Muto, J., Nakatani, T., Nishikawa, O., & Nagahama, H. (2015). Fractal particle size distribution of pulverized fault rocks as a function of distance from the fault core. *Geophysical Research Letters*, *42*, 3811–3819. https://doi.org/10.1002/2015GL064026

Okada, Y. (1985). Surface deformation due to shear and tensile faults in a half-space. *Bulletin of the Seismological Society of America*, *75*(4), 1135–1154.

Okubo, P. G., & Aki, K. (1987). Fractal geometry in the San Andreas Fault System. *Journal of Geophysical Research*, *92*(B1), 345–355. https://doi.org/10.1029/JB092iB01p00345

Oliver, M., & Webster, R. (2014). A tutorial guide to geostatistics: Computing and modelling variograms and kriging. *CATENA*, *113*, 56–69. https://doi.org/10.1016/J.CATENA.2013.09.006

Omori, F. (1894). On the aftershocks of earthquakes. *Journal of the College of Science, Imperial University of Tokyo*, *7*, 111–200.

Page, M. T., Custódio, S., Archuleta, R. J., & Carlson, J. M. (2009). Constraining earthquake source inversions with GPS data: 1. Resolution-based removal of artifacts. *Journal of Geophysical Research*, *114*, B01314. https://doi.org/10.1029/2007JB005449

Parsons, T., & Minasian, D. L. (2015). Earthquake rupture process recreated from a natural fault surface. *Journal of Geophysical Research: Solid Earth*, *120*, 7852–7862. https://doi.org/10.1002/2015JB012448

Passelègue, F. X., Schubnel, A., Nielsen, S., Bhat, H. S., Deldicque, D., & Madariaga, R. (2016). Dynamic rupture processes inferred from laboratory micro-earthquakes. *Journal of Geophysical Research: Solid Earth*, *121*, 4343–4365. https://doi.org/10.1002/2015JB012694

Perrin, C., Manighetti, I., Ampuero, J.-P., Cappa, F., & Gaudemer, Y. (2016). Location of largest earthquake slip and fast rupture controlled by along-strike change in fault structural maturity due to fault growth. *Journal of Geophysical Research: Solid Earth*, *121*, 3666–3685. https://doi.org/10.1002/2015JB012671

Poon, C. Y., Sayles, R. S., & Jones, T. A. (1992). Surface measurement and fractal characterization of naturally fractured rocks. *Journal of Physics D: Applied Physics*, *25*(8), 1269–1275. https://doi.org/10.1088/0022-3727/25/8/019

Power, W. L., Tullis, T. E., & Weeks, J. D. (1988). Roughness and wear during brittle faulting. *Journal of Geophysical Research*, *93*, 15,268–15,278. https://doi.org/10.1029/JB093iB12p15268

Powers, P. M., & Jordan, T. H. (2010). Distribution of seismicity across strike-slip faults in California. *Journal of Geophysical Research*, *115*, B05305. https://doi.org/10.1029/2008JB006234

Renard, F., Voisin, C., Marsan, D., & Schmittbuhl, J. (2006). High resolution 3D laser scanner measurements of a strike-slip fault quantify its morphological anisotropy at all scales. *Geophysical Research Letters*, *33*, L04305. https://doi.org/10.1029/2005GL025038

Roberts, G. O., Gelman, A., & Gilks, W. R. (1997). Weak convergence and optimal scaling of random walk metropolis algorithms. *The Annals of Applied Probability*, *7*(1), 110–120. https://doi.org/10.1214/aoap/1034625254

Robertson, M. C., Sammis, C. G., Sahimi, M., & Martin, A. J. (1995). Fractal analysis of three-dimensional spatial distributions of earthquakes with a percolation interpretation. *Journal of Geophysical Research*, *100*(B1), 609–620. https://doi.org/10.1029/94JB02463

Sagy, A., Brodsky, E. E., & Axen, G. J. (2007). Evolution of fault-surface roughness with slip. *Geology*, *35*(3), 283. https://doi.org/10.1130/G23235A.1

Sambridge, M. (1999). Geophysical inversion with a neighbourhood algorithm-II. Appraising the ensemble. *Geophysical Journal International*, *138*(3), 727–746. https://doi.org/10.1046/j.1365-246X.1999.00900.x

Shi, Z., & Day, S. M. (2013). Rupture dynamics and ground motion from 3-D rough-fault simulations. *Journal of Geophysical Research: Solid Earth*, *118*, 1122–1141. https://doi.org/10.1002/jgrb.50094

Tarantola, A. (2005). *Inverse problem theory and methods for model parameter estimation* (2nd ed., pp. 50–52). Philadelphia: Society for Industrial and Applied Mathematics. https://doi.org/10.1137/1.9780898717921.ch2

USGS (2006). Quaternary fault and fold database for the United States.

von Kármán, T. (1948). Progress in the statistical theory of turbulence. *Proceedings of the National Academy of Sciences of the United States of America*, *34*(11), 530–9.

Walters, R. J., Elliott, J. R., D'Agostino, N., England, P. C., Hunstad, I., Jackson, J. A., et al. (2009). The 2009 L'Aquila earthquake (Central Italy): A source mechanism and implications for seismic hazard. *Geophysical Research Letters*, *36*, L17312. https://doi.org/10.1029/2009GL039337

Wang, L., Hainzl, S., & Mai, P. M. (2015). Quantifying slip balance in the earthquake cycle: Coseismic slip model constrained by interseismic coupling. *Journal of Geophysical Research: Solid Earth*, *120*, 8383–8403. https://doi.org/10.1002/2015JB011987

Wei, S., Barbot, S., Graves, R., Lienkaemper, J. J., Wang, T., Hudnut, K., et al. (2015). The 2014 Mw 6.1 South Napa earthquake: A unilateral rupture with shallow asperity and rapid afterslip. *Seismological Research Letters*, *88*, 344–354.

Wesnousky, S. (1988). Seismological and structural evolution of strike-slip faults. *Nature*, *335*, 340–343. https://doi.org/10.1038/335340a0

Wesnousky, S. (2006). Predicting the endpoints of earthquake ruptures. *Nature*, *444*, 358–360. https://doi.org/10.1038/nature05275

Wessel, P., & Smith, W. H. F. (1991). Free software helps map and display data. *Eos, Transactions American Geophysical Union*, *72*, 441.

Weston, J., Ferreira, A. M., & Funning, G. J. (2011). Global compilation of interferometric synthetic aperture radar earthquake source models: 1. Comparisons with seismic catalogs. *Journal of Geophysical Research*, *116*, B08408. https://doi.org/10.1029/2010JB008131

Wright, T. J. (2003). Source model for the M_W 6.7, 23 October 2002, Nenana Mountain Earthquake (Alaska) from InSAR. *Geophysical Research Letters*, *30*, 1974. https://doi.org/10.1029/2003GL018014

Xu, X., Tong, X., Sandwell, D. T., Milliner, C. W., Dolan, J. F., Hollingsworth, J., et al. (2016). Refining the shallow slip deficit. *Geophysical Journal International*, *204*(3), 1843–1862. https://doi.org/10.1093/gji/ggv563

Zhang, L., Mai, P. M., Thingbaijam, K. K., Razafindrakoto, H. N., & Genton, M. G. (2015). Analysing earthquake slip models with the spatial prediction comparison test. *Geophysical Journal International*, *200*(1), 185–198. https://doi.org/10.1093/gji/ggu383

Zhang, Y., Wang, R., & Chen, Y.-T. (2015). Stability of rapid finite-fault inversion for the 2014 M_W 6.1 South Napa earthquake. *Geophysical Research Letters*, *42*, 10,263–10,272. https://doi.org/10.1002/2015GL066244